Article:
Zhang, M. orcid.org/0000-0002-1094-7279, Shi, Y., Koval, V. et al. (7 more authors) (2025) Direct magnetoelectric coupling from magnetically/ferroelectrically active cation in low-symmetry octahedron. Physical Review B, 112. 054423. ISSN: 2469-9950

https://doi.org/10.1103/h4kv-qszp

Direct magnetoelectric coupling from magnetically/ferroelectrically active cation in low symmetric octahedron

Man Zhang[1], Yu Shi[2, 3], Vladimir Koval[4], Yajun Yue[5], Zixuan Wu[3], Yongyi Wu[6], Yuqing Zhou[6], Tao Li[6], Chenglong Jia[2,7*], Haixue Yan[3]

[1] School of Mechanical Engineering, University of Leeds, Woodhouse, Leeds, LS2 9JT, UK

[2] School of Physical Science and Technology, Lanzhou University, Lanzhou 730000, China

[3] School of Materials Science and Engineering, Queen Mary University of London, Mile End Road, London, E1 4NS, UK

[4] Institute of Materials Research, Slovak Academy of Sciences, Watsonova 47, 040 01 Kosice, Slovakia

[5] School of Chemistry, South China Normal University (SCNU), Guangzhou 510006, Guangdong, China

[6] Center for Spintronics and Quantum Systems, State Key Laboratory for Mechanical Behavior of Materials, Department of Materials Science and Engineering, Xi'an Jiaotong University, Xi'an 710049, China

[7] Lanzhou Center for Theoretical Physics, Key Laboratory of Theoretical Physics of Gansu Province, and Key Laboratory of Quantum Theory and Applications of MoE, Lanzhou University, Lanzhou 730000, China

Email: cljia@lzu.edu.cn

Abstract

Achieving direct and large magnetoelectric (ME) coupling in single-phase multiferroic at room temperature is a challenging task for physicists and material engineers as Type-I multiferroics have independent ferroic orders and Type-II multiferroics exhibit fairly weak polarization due to spin-orbit interaction at very low temperatures. Here, we show that by lowering the symmetry of $BiFeO_3$ via the oxygen octahedron distortion and proper tilting it is possible to induce the spontaneous polarization from B-site Fe ions and a partial reduction of Fe^{3+} into Fe^{2+} results in ferromagnetic super-exchange Fe^{3+}-O-Fe^{2+}interactions, providing room temperature multiferroics that have the same origin for both ferroelectricity and ferromagnetism. The dynamic room-temperature ME effect which originates from the intrinsic ME interaction between magnetic moments and ferroelectric polarization is evidenced by the resonant behavior of the complex dielectric permittivity and complex magnetic permeability at microwaves. A striking interplay between ferroelectricity and magnetism is demonstrated by the electric polarization reversal and magnetization reversal, both actuated by applied magnetic and electric fields. The new room-temperature multiferroic material combines the advantages of Type-I multiferroics and Type-II multiferroics, providing thus great potential for construction of low-energy non-volatile magnetoelectric storages and sensors.

Key words: perovskite, room-temperature multiferroic; intrinsic magnetoelectric coupling; $BiFeO_3$

Introduction

The ability of magnetoelectric (ME) multiferroics to couple magnetic and ferroelectric orders suggests that they have the potential to add functionality to devices while also reducing energy consumption [1–3]. However, it is extremely difficult to develop room temperature single phase multiferroics. The current challenges include[4–6]: 1) The small polarization of spin origin and relatively low magnetic (spiral) ordering temperatures rule out nearly all Type-II multiferroics for ambient working temperature; 2) $BiFeO_3$-based Type-I multiferroics exhibit prominent displacive ferroelectricity along with antiferromagnetism above room temperature[7]. However, $BiFeO_3$ (BFO) exhibit weak magnetic properties (canted ferromagnetism) and ME coupling coefficient at ambient temperature due to the independent origins of the ferroic orders[8].

Ideal multiferroics should combine the advantages of both type-I and Type-II multiferroics, where one-cation in a single-phase multiferroic is responsible for both ferroelectricity and ferromagnetism. However, this is usually challenging as it goes beyond the d^0 rule between *d*-electrons and ferroelectricity for multiferroics of type-I[9].

Entanglement of the crystal symmetry, spin–orbit and magnetic order in multiferroic materials is currently one of the most exciting fields of research and bears a strong potential for engineering novel electronic devices. The broken symmetry in ferroelectrics which is caused by the generation of spontaneous polarization can lead to a spin splitting of the electronic band structure. This phenomenon has been observed in polar semiconductor BiTeI[10], the polar surface of $SrTiO_3$[11] and high Z-surface alloys[12]. The spin-orbit state is directly linked to the magnetic property of a material. For example, interfacial magnetic state was observed in non-ferromagnetic $SrTiO_3$ film [13,14]. The magnetic state was attributed to the existence of oxygen vacancies which leads to orbital reconstruction and generates a two-dimensional interface magnetic state. Recent research on $Ge_{1-x}Mn_xTe$[15] and (In,Fe)As[16] have reported ferromagnetic order caused by spin–splitting in both materials.

Similar to above mentioned materials, it is possible to tune the magnetic state in BFO by designing the local polarization structure and hence spin state. In pure BFO with rhombohedral structure where ferroelectric spontaneous polarization comes from displacement of Bi^{3+}, all the six oxygen atoms share the same position in the FeO_6 oxygen octahedron[17], which is same with the oxygen octahedron in a cubic structure. As is demonstrated in **Fig. 1a**, for cubic structured FeO_6, the five *d*-orbitals of Fe split into e_g and t_{2g} states. In a low symmetric tetragonal unit cell where Fe moves away from the body center, the e_g state further splits into a_1 and b_2 states, while the t_{2g} states split into e and b_2 states. Due to the difference between crystal-field splitting energy (Δ ~ 1 eV) and on-site coulomb interaction energy (U ~ 3-5 eV), both cubic and tetragonal structures exhibit a ground high-spin state for Fe ions[18,19]. Experimentally, introducing oxygen vacancies or other means allows for the presence of both Fe^{3+} and Fe^{2+} in FeO_6 octahedrons. As a result, following the Goodenough-Kanamori rules that a (nearly) 180° superexchange coupling between a half-filled *d*-orbital and a fully-filled *d*-orbital can be strongly ferromagnetic; thus, ferromagnetism arises from Fe^{3+}-O- Fe^{2+} bonds. Together with the spontaneous polarization resulting from displacements of Fe and apical O ions in tetragonal structured FeO_6, one can have both ferroelectricity and ferromagnetism originating from Fe ions at B sites in the perovskites, in contrast to pure BFO with the nearly independent origins of the ferroic orders from A and B sites respectively. Furthermore, the small orbital splitting caused by the tetragonal distortion of FeO_6 will enhance the sensitivity of multiferroic orders, giving rise to a strong ME response of tetragonal structured FeO_6 octahedrons.

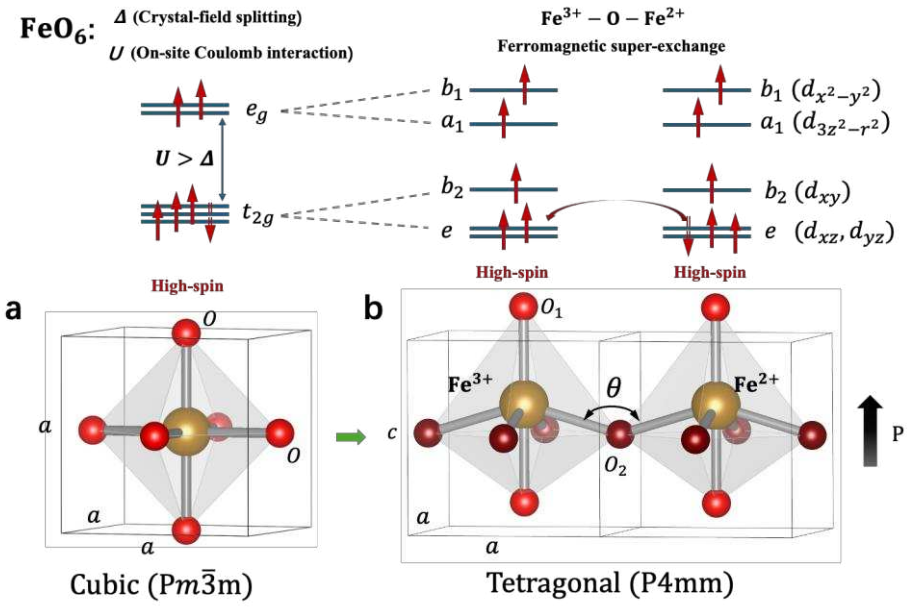

Fig. 1 Schematic for multiferroicity of distorted FeO_6 octahedrons. In both (**a**) cubic and (**b**) tetragonal structures, Fe^{3+} and Fe^{2+} are in their ground high spin states because of a larger Hubbard U compared to the crystal-field splitting Δ. In the low symmetric tetragonal structure, the ferromagnetic superexchange interaction between Fe^{3+}-O-Fe^{2+} with an angle θ leads to the coexistence of ferromagnetism and ferroelectricity (spontaneous polarization P from displaced Fe and apical O ions). Manipulating the angle θ offers possibilities for controlling the magnetoelectric properties of distorted FeO_6 octahedrons.

In this paper, we aim to overcome current limitations in experiments and exploit the potential of combining the advantages of Type I and II multiferroics in $BiFeO_3$-$BaTiO_3$-$Bi_{0.5}Na_{0.5}TiO_3$ (BFO-BT-BNT) solid solutions at room temperature. By doping BFO with $BaTiO_3$ (BT) and $Bi_{0.5}Na_{0.5}TiO_3$ (BNT), the symmetry of FeO_6 could be effectively distorted or lowered, which could induce finite local ferroelectric polarization through displacement of magnetically active Fe ions. At the same time, the local chemical properties of FeO_6 will be modified to incorporate both Fe^{3+} and Fe^{2+}, thereby introducing ferromagnetic super-exchange interactions between Fe^{3+}-O-Fe^{2+} as predicted by the Goodenough-Kanamori rule. The results show that the developed new ceramics show intrinsic ME coupling which originates from

resonant dynamics of magnetic moments and ferroelectric polarization at GHz frequency. The electric polarization and ferromagnetic magnetization can be effectively controlled with magnetic fields and electric fields. Our work not only add new room temperature multiferroic materials, but also point to a unique mechanism to engineer multiferroics.

Results and discussion

Crystal structure and chemical states of BFO-based ceramics

$BiFeO_3$-$BaTiO_3$ based ceramics with different $Bi_{0.5}Na_{0.5}TiO_3$ content were synthesized. The ceramics have a general formula of $(0.67\text{-}x)Bi_{0.99}La_{0.01}FeO_3\text{-}0.33BaTiO_3\text{-}xBi_{0.5}Na_{0.5}TiO_3$ (x = 0, 0.02, 0.04 and 0.06) and are abbreviated as BFO-BT-100xBNT. The relative densities of the sintered ceramic pellets were determined by the Archimedes method and found to be above 95%, which indicates a good quality of the ceramics. The microstructures and elemental distributions for all the ceramics are shown by the respective SEM and EDX images in Fig. S1, in the Supplemental Material [20] (including reference [21]). The spatial distribution of Bi, Fe, Ba, Ti, Na atoms and oxygen within grains is homogeneous, except for the BFO-BT-6BNT ceramic, where (Ba,Ti)-rich areas exist, suggesting a limited solubility of BT in the solid solution system. Therefore, the BFO-BT-6BNT sample was excluded from our further study.

From the earlier studies on crystal structure of BFO-BT-0BNT, it is expected that the investigated ceramics consist of a rhombohedral (*R*) phase[22], a tetragonal (*T*) phase[23] and a cubic (*C*) phase[24], or it can be a combination of different phases, depending on the BT content[25]. In this work, tetragonal *P*4*mm* and cubic *Pm*-3*m* models were used to refine the XRD patterns of BFO-BT-100xBNT ceramics[26,27]. Excellent fits were obtained for the powder XRD patterns (**Fig. 2**), with the refinement parameters listed in Table S1[20]. To present the differences between observed and calculated profiles, all plots are shown with logarithm scale of y-axis. The crystal structure of the BFO-BT-0BNT (33% BT) sample is dominated by the cubic phase with a small fraction of the tetragonal phase (10.36%). With increased BNT content, the weight fraction

(W_p) of tetragonal phase significantly increases (Table S1)[20], leading to dominant tetragonal structure in the BFO-BT-2BNT and BFO-BT-4BNT samples. Here the weight fraction was calculated through $W_p = \frac{S_p m_p}{\sum_{p=1}^{N_p} S_{ph} m_p}$, where S_p is the refined phase fraction scale for phase p, m_p is the unit cell mass, and N_p is the total number of phases ($N_p = 2$). However, it is worth noting that the crystallographic models only present averaged structural features, which means local-scale chemical heterogeneity and atom-dependent distortions are hard to be evaluated based on powder diffraction data only.

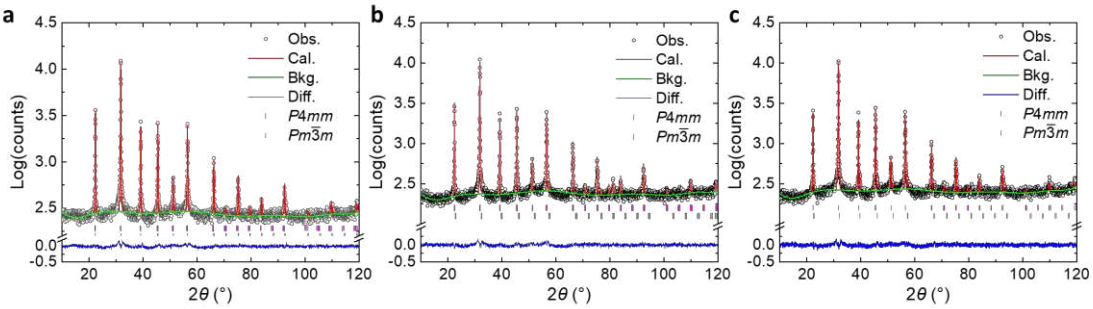

Fig. 2 Fitted X-ray powder diffraction profiles of BFO-BT-100xBNT ceramics. **a)** BFO-BT-0BNT; **b)** BFO-BT-2BNT and **c)** BFO-BT-4BNT.

Table 1 Phase composition of BFO-BT-100xBNT ceramics.

	BFO-BT-0BNT	BFO-BT-2BNT	BFO-BT-4BNT
Phase 1	Tetragonal (*P*4*mm*)	Tetragonal (*P*4*mm*)	Tetragonal (*P*4*mm*)
Weight fraction	0.103(7)	0.899(1)	0.967(3)
Phase 2	Cubic ($Pm\bar{3}m$)	Cubic ($Pm\bar{3}m$)	Cubic ($Pm\bar{3}m$)
Weight fraction	0.897(1)	0.101(1)	0.033(7)

Chemical states of Fe and O elements in the BFO-BT-100xBNT ceramics were characterized by XPS. As is shown in Fig. S2,[20] the Fe 2*p* peak for all the ceramics was deconvoluted into Fe^{2+} and Fe^{3+} peaks. It is worth noting that the fitted XPS spectra in Fig. S2 is only to show the presence of Fe^{2+}, not for quantitative analysis. This is because using Fe 2*p* peaks to quantitatively analysis of Fe^{3+} and Fe^{2+} will introduce large uncertainty due to the

overlap between the two main peaks (Fe 2*p*3/2 and Fe 2*p*1/2) and the satellite peaks. The reduction of Fe^{3+} into Fe^{2+} in the ceramics will lead to the generation of oxygen vacancies. The O 1*s* XPS peaks which were normalized to the Ba 3*d* intensity of all the ceramics are shown in **Fig. 3**. Ba is chosen as it remains inert during the reduction reaction (Ba 3*d* spectra shown in Fig. S2).[20] Notably, with increasing BNT content the normalized O 1*s* XPS intensity began to increase, and the XPS peak position moved to lower binding energies, suggesting a decreasing concentration of oxygen vacancies[21]. The detailed data for O 1*s* XPS spectra are summarized in Table S3.

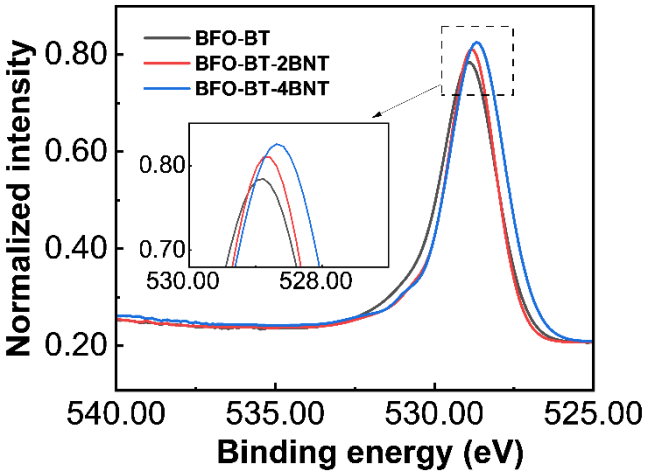

Fig. 3 Normalized O 1*s* XPS spectra of the BFO-BT-100xBNT ceramics

Ferroelectric and ferromagnetic properties

The dielectric, ferroelectric and magnetic properties of the BFO-BT-100xBNT ceramics are presented in **Fig. 4**. The temperature dependence of the relative dielectric permittivity (ε) of the ceramics before (solid lines) and after poling (dashed lines) shows a broad and frequency dependent permittivity peak, suggesting the relaxor behavior due to polar nanodomains (Fig 4a1 - Fig. 4c1)[28]. After poling, the dielectric permittivity *vs.* temperature curves of all the ceramics show diffusion-like features, with the ferroelectic Curie point spanning the temperature range 350 - 400 °C. With BNT content increases, the temperature

corresponding to maximum dielectric permittivity of BFO-BT-100xBNT shifts to low temperature, which is consistent with the decrease of tetragonal distortion (c/a) in Table S1. The dramatic increase in permittivity after poling points to the electric field-induced irreversible phase transition from a weak polar state to a strong polar state [29]. The increased permittivity can also be seen in the frequency spectra (Fig. S3)[20]. Electric field induced phase transition has been reported in ferroelectric ceramics where an increase in dielectric permittivity after electric poling is found[30,31]. During poling process, the applied electric field can: 1) drive domain switching to reduce domain wall density and 2) work as driving force for phase transition from weak polar to strong polar. In the first case, dielectric permittivity of the ceramic will decrease after poling due to the decrease in domain wall density. In the second case, the dielectric permittivity which is related to crystal structure of the material might increase. The resonance peaks on the frequency-dependent permittivity and loss curves of the poled ceramics are indicative of piezoelectricity, and thus the field-induced domain switching. Modified Curie Weiss law[32] was used to characterize the diffusion behavior of all the ceramics. The results (Figure S4)[20] show that, with increasing BNT content, the ceramics become more diffused, as indicated by increasing γ values.

Fig. 4 (a2-c2) displays the electrical displacement *vs*. electric field (*D*-*E*) and electrical current *vs*. field (*I*-*E*) loops of the investigated ceramics, as measured at room temperatures at a frequency of 10 Hz. Even that the *D*-*E* loops are not fully saturated, a typical hysteresis behavior of the electrical displacement is clearly observed. In addition, four current peaks (indicated by arrows), which are located in the first and third quadrants, can be identified on the *I*-*E* loops. As the current peaks in I-E loops are not located at the highest applied field, we can confirm that the dominated contrition in D-E loops is not due to conductivity contribution (or loss contribution)[33]. According to the previous ferroelectric studies on similar relaxor

systems[33], the electric fields of the four current peaks correspond to the fields necessary for the electric field-induced irreversible phase transition and domain switching[34].

The characteristic dielectric and piezoelectric parameters of the BFO-BT-100xBNT ceramics are given in Table S4 in ref [20]. Compared to BFO-BT-0BNT, the BFO-BT-2BNT and BFO-BT-4BNT ceramics show the improved dielectric and piezoelectric properties. The increase in the permittivity can be attributed to the increased polar phase, which coincides with the dominance of the polar tetragonal phase (Table 1) in the BFO-BT-2BNT and BFO-BT-4BNT ceramics. The higher piezoelectric coefficient d_{33} in these samples can be explained by the increased relative dielectric permittivity in accordance with the expression: $d_{33} = 2Q\varepsilon_0\varepsilon_r P_r$, where Q is the electrostrictive coefficient, ε_0 is permittivity of vacuum, ε_r is the relative dielectric permittivity and P_r is the remnant polarization[35,36].

Fig. 4a3 shows the dependencies of magnetization on magnetic field for the BFO-BT-0BNT, BFO-BT-2BNT and BFO-BT-4BNT ceramics. The non-linear behavior of the magnetization represented by the magnetization - magnetic field (*M-H*) loops and the non-zero remnant magnetization indicate that all the ceramics are ferromagnetic materials at room temperature. The temperature dependencies of the magnetization from room temperature up to 625 °C are shown in **Fig. 4b3**. The ferromagnetic Curie temperature (T_c) for each composition was obtained by the first derivative of magnetization with respect to temperature (the inset of Fig. 4b3). It was found that as BNT content increases, T_c rises from 355.8 °C (BFO-BT-0BNT) through 361.7 °C (BFO-BT-2BNT) to 374.7 °C (BFO-BT-4BNT). The robustness of T_c against significant changes in crystal structures caused by BNT content (cf. Table I) suggests a common origin for ferromagnetism in BFO-BT-0BNT, BFO-BT-2BNT and BFO-BT-4BNT. According to the semi-empirical Goodenough-Kanamori rules, one can assume that ferromagnetism in these ferrite-based ceramics is primarily due to ferromagnetic super-exchange interactions between Fe^{2+} and Fe^{3+} ions. [37] As mentioned earlier, with increasing the

BNT content, the oxygen vacancy concentration decreases, which is related to decreased content of Fe^{2+}. A monotonically decreasing percentage of Fe^{2+} within these ceramics might be the reason for weakened saturated magnetization in BFO-BT-0BNT, BFO-BT-2BNT and BFO-BT-4BNT (**Fig. 4c3**).

The observed ferroelectric and ferromagnetic behaviours indicate that all the investigated ceramics are multiferroics at room temperature. Moreover, the ferromagnetic coupling is expected to be intrinsic as the Fe ions at the B-sites contribute to both the spontaneous polarization (due to the polar tetragonal structure) and the spontaneous magnetization.

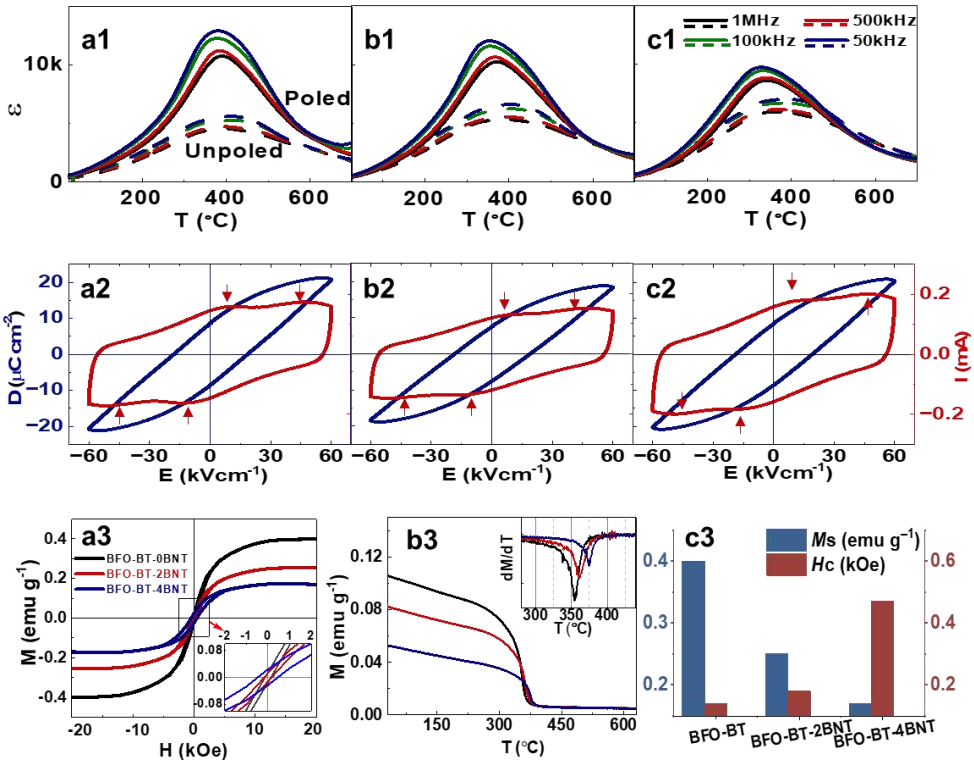

Fig. 4 Dielectric, ferroelectric and magnetic properties of the BFO-BT-0BNT, BFO-BT-2BNT, BFO-BT-4BNT ceramics. **a1-c1**: temperature dependence of the relative dielectric permittivity (ε) at different frequencies before (solid line) and after (dashed line) poling. **a2-c2**: displacement – current - electric field (*D-I-E*) curves measured at room temperature under 10 Hz; **a3:** magnetization - magnetic field (*M-H*) hysteresis loops measured under 20 kOe

(inset: enlarged M-H loops); **b3**: temperature dependence of magnetization and the first derivative of magnetization dM/dT with respect to temperature, showing the ferromagnetic Curie temperature (insert of **b3**); **c3**: saturated magnetization (M_s) and coercive magnetic field (H_c), as obtained from the recorded *M-H* loops at room temperature. The uncertainties for *M*s are 0.015 emu g^{-1}, 0.013 emu g^{-1} and 0.002 emu g^{-1}, and the uncertainties for *H*c are 17 Oe, 39 Oe and 32 Oe for BFO-BT-0BNT, BFO-BT-2BNT, BFO-BT-4BNT, respectively.

Intrinsic magnetoelectric coupling

The advantage of magnetoelectric multiferroics is a striking interplay between ferroelectricity and magnetism, which provides new possibilities to manipulate their functional properties. An important and promising way to characterize the intrinsic magnetoelectric coupling in a multiferroic material is through investigating resonant dynamics, where the magnetoelectric interaction can be strongly enhanced via collective ferroelectric and magnetic excitation modes[38]. The basic condition for the resonance to occur is that spin excitations and fluctuations of polarization are simultaneously activated by magnetic and electric fields. In such a case, electromagnon spin waves will emerge and bring about an anomaly in the complex dielectric permittivity and complex magnetic permeability[39,40]. **Fig. 5** displays the frequency dependence of the real and imaginary parts of the complex dielectric permittivity ($\varepsilon(f) = \varepsilon'(f) + i\varepsilon''(f)$) and complex magnetic permeability ($\mu(f) = \mu'(f) + i\mu''(f)$) of the investigated ceramics at microwaves. For the BFO-BT-0BNT sample, a series of resonance peaks can be observed on the ε(f) and μ(f) plots. In the GHz region, the permittivity is mainly contributed by dipolar polarization rather than space charges[38]. The resonance peaks on the $\varepsilon''(f)$ curve originate likely from the intrinsic lattice polarization and the defect dipole effects linked with oxygen vacancies[41]. The resonance peaks observed on the $\mu''(f)$ curve can be related to the intrinsic magnetic resonance and exchange resonance (spin waves) modified by

defects. For the BFO-BT-2BNT sample, only one resonance peak, centred at ~ 11.5 GHz, is observed on the $\mu''(f)$ plot, and its intensity is the highest of all the investigated compositions. The resonance permittivity peak can be attributed to the intrinsic polarization and the resonance magnetic permeability originates from the intrinsic magnetic moments. It is worth noting that the resonant frequency of the dielectric permittivity matches well with that of the magnetic permeability. Given that the strain-mediated magnetoelectric coupling typically shifts the magnetic resonance frequency due to effective magnetic anisotropy[42], the identical resonant frequency of the dielectric permittivity and magnetic permeability peaks suggests a linear intrinsic magnetoelectric coupling as both time-reversal and inversion symmetry are simultaneously broken[43]. Similar to the BFO-BT-0BNT ceramic, the BFO-BT-4BNT sample shows a series of the resonance dielectric permittivity and magnetic permeability peaks. The additional peaks in BFO-BT-0BNT possibly can be attributed to its high oxygen vacancies[44] (**Fig. 3**). The additional peaks in BFO-BT-4BNT are possibly due to its strong diffusion nature at Tc, reflected by its high value of γ (Table S4), which has local polar regions with different relaxation time[45,46]. Although further detailed clarification is needed for this direct ME coupling in single crystalline samples, these results imply that the mixed valence of Fe (Fe^{2+}/Fe^{3+}) at the B-sites is crucial for realizing viable BFO-based magnetoelectric multiferroics.

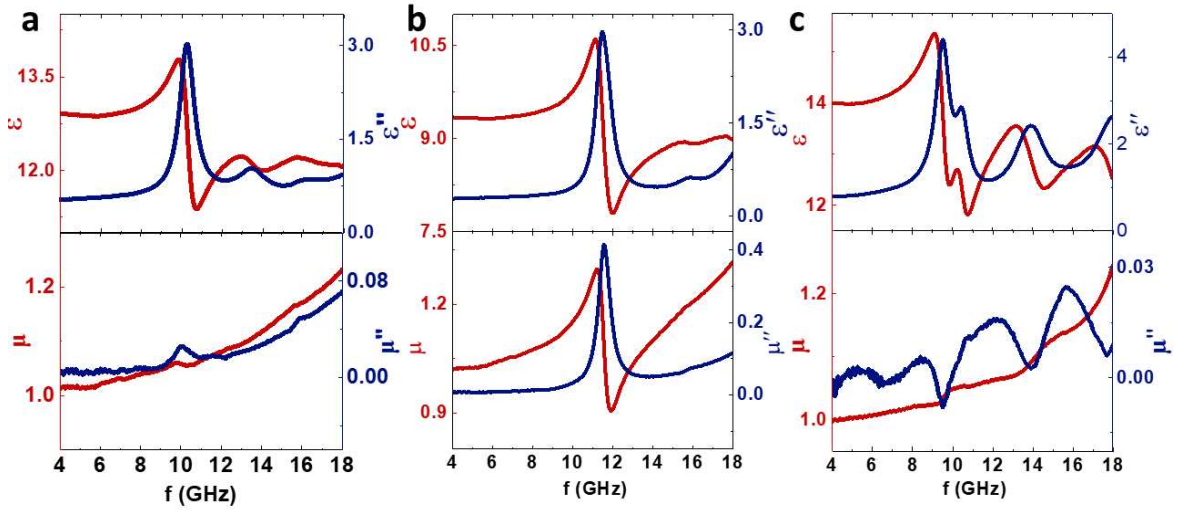

Fig. 5 Intrinsic magnetoelectric coupling characterized by the resonant behavior of the complex dielectric permittivity and complex magnetic permeability at microwaves. **a)** BFO-BT-0BNT; **b)** BFO-BT-2BNT and **c)** BFO-BT-4BNT.

Electrical polarization controlled by a magnetic field and magnetization changes in an external electric field

The strong magnetoelectric effect in BFO-BT-2BNT ceramic was further studied by piezoresponse force microscopy (PFM) and magnetic force microscopy (MFM). PFM images of the ceramic subjected to various electric and magnetic fields are presented in **Fig. 6**. **Fig. 6a** shows the phase change of BFO-BT-2BNT under ±10 V, ±20 V and ±30 V. After applying an increasing negative and positive DC bias over the square areas of 5 × 5 μm^2 and 3 × 3 μm^2, the obtained phase maps clearly demonstrate the electric field-induced polarization switching and transitions, which is consistent the four current peaks in the I-E loops in Fig 4 (a2-c2). The polarization switching originates from Bi^{3+} related spontaneous polarization in $BiFeO_3$ and Ba^{2+} related spontaneous polarization in $BaTiO_3$. The piezoresponse phase change excited by different magnetic fields is shown in **Fig. 6b**. From the LPFM (Lateral Piezoresponse Force Microscopy) phase images, it is obvious that a magnetic field of +8000 Oe initiates polarization switching in the sample. Reversing the magnetic field (-8000 Oe) causes flipping of the polarization direction (marked by the blue arrows in **Fig. 6b**). The application of a magnetic field can effectively align the magnetic spins, and, through ME coupling, the direction of electric polarization is changed by applied magnetic field. Thus, the electrical property of the BFO-BT-2BNT ceramic can be controlled by the external magnetic field. **Fig. 6c** displays the *P* - *E* loops recorded at the marked spot *P* before and after being magnetized under a magnetic field of 800 Oe. It is obvious that the *P* - *E* loops are saturated, with an increase in the coercive electric field (*Ec*) after magnetization. The polarization reversal is a multi-step process,

including growth of existing domains, domain wall motion and nucleation and growth of anti-parallel domains[47,48]. The changes in the electrical coercive field are related to variations in the domain wall density. Higher magnetic fields facilitate the growth of ferroelectric domains, leading to a lower domain wall density and, thus, the increased coercive electric field[48,49].

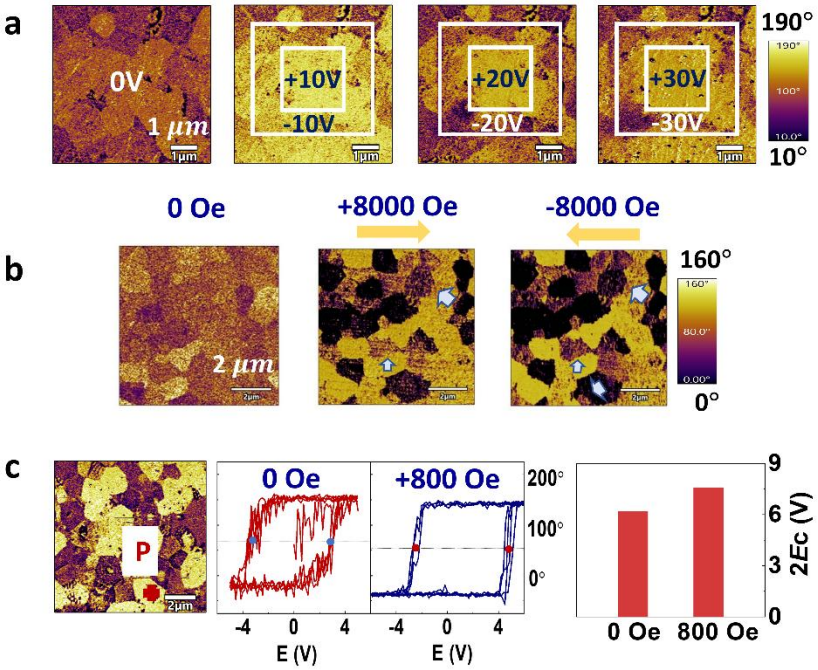

Fig. 6 Controlling of polarization by external electric and magnetic fields. **a)** PFM phase images of the BFO-BT-2BNT ceramic under different electric fields (0 V, ±10 V, ±20 V and ±30 V); **b)** PFM phase images of the BFO-BT-2BNT ceramic under different magnetic fields (0 Oe, + 8000 Oe and -8000 Oe) and **c)** PFM phase image and *P-E* loops recorded before and after being magnetized at +800 Oe, together with the electric coercive field extracted from the *P-E* loops. The standard deviation for *Ec* in **c)** is ±0.22 V and ±0.08 V for *P-E* loops measured under applied magnetic field of 0 Oe and 800 Oe.

The controlling of magnetic properties by an external electrical field in the BFO-BT-2BNT ceramic is demonstrated in **Fig. 7**. Fig. 7(a1-c1) shows the MFM images of the virgin sample, where weak magnetic features can be observed on the nanometer scale. After poling

at a DC voltage of 20 V (Fig. 7(a2-c2)), magnetic domains of an average size of ~ 1 μm are clearly visible in the MFM images. However, no distinct ferroelectric domain walls can be found in the sample by PFM (Fig. 7(a3-c3)), which can be attributed to its relaxor ferroelectric nature associated with the ferroelectric nanodomains. It is reasonable to assume that the MFM contrast in Fig. 7(a2-c2) originates from the ferromagnetic domains and/or possible surface charge. To investigate the electric field gradient distribution above the sample surface, Electric Force Microscopy (EFM) technique was employed. The observed contrasts in the EFM images (Fig. 7(a4-c4)) confirm the accumulation of charges on the surface of the ceramic. A subtraction of the EFM signal (Fig. 7(a4-c4)) from the MFM signal after DC poling provides the real ferromagnetic signal (Fig. 7(a2-c2)), which is dramatically different from that before poling. The application of an electric field can drive electric polarization switching (indicated by Fig. 7b3 and Fig. 4b2). The ME coupling will lead to ferromagnetic domain orientation, which is reflected by the change in MFM images before and after DC poling.

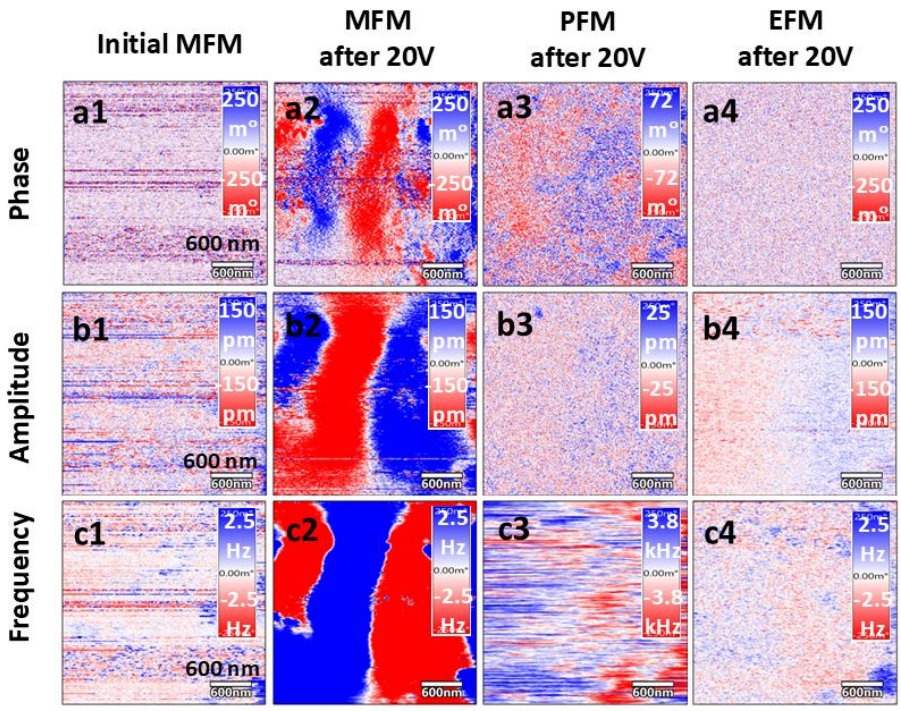

Fig. 7 Controlling of ferromagnetic domains by an external electric field. **a1-c1)** initial MFM images showing ferromagnetic signals; **a2-c2)** MFM images after DC poling; **a3-c3)** PFM

images after DC poling showing ferroelectric signals; **a4**-**c4)** EFM images after DC poling showing the electric field gradient distribution; **a1**-**a4)** phase; **b1**-**b4)** amplitude and **c1**-**c4)** frequency.

Conclusions

Room-temperature multiferroic (0.67-x)$Bi_{0.99}La_{0.01}FeO_3$-0.33$BaTiO_3$-x$Bi_{0.5}Na_{0.5}TiO_3$ (BFO-BT-100xBNT, x = 0, 0.02, 0.04) ceramics with same origin of ferroelectricity and magnetism were prepared by the conventional solid state reaction method. The BFO-BT-0BNT, BFO-BT-2BNT and BFO-BT-4BNT ceramics adopt a biphasic structure composed of cubic and tetragonal phases. The electrical displacement of Fe ions at B-sites was found to be responsible for the spontaneous polarization and its hysteresis in an external electric field. In addition, a magnetization hysteresis, characteristic of ferromagnetic ceramics, was observed at room temperature for all the ceramics under consideration. The ferromagnetism is suggested to originate from the superexchange interaction of the B-site Fe^{2+} and Fe^{3+} ions. For the representative BFO-BT-2BNT ceramic, the intrinsic magnetoelectric coupling was evidenced at room temperature by the resonant behavior of the complex dielectric permittivity and complex magnetic permeability in the GHz region. The existence of the room-temperature magnetoelectric coupling and inverse magnetoelectric effect in the multiferroic material was further confirmed by piezoresponse force microscopy and magnetic force microscopy under applied magnetic and electric fields. The present work offers a unique method to obtain single-phase magnetoelectric multiferroics via the engineering of the electronic and crystal structures of $BiFeO_3$-based perovskite oxides.

Methods

(0.67-x)$Bi_{0.99}La_{0.01}FeO_3$-0.33$BaTiO_3$-x$Bi_{0.5}Na_{0.5}TiO_3$ (hereinafter abbreviated as BFO-BT-100xBNT, x = 0, 0.02, 0.04, 0.06) ceramics were prepared by the conventional solid state reaction method. Stoichiometric quantities of Bi_2O_3 (purity: 99.975%), La_2O_3 (99.99%), Fe_2O_3 (99.945%), $BaCO_3$ (99.8%), TiO_2 (99.0%), Na_2CO_3 (99.5%) were mixed together using a planetary ball milling machine (Nanjing machine factory, China). The ball milling process was carried out for 4 hrs at a speed of 170 rpm. The slurry was dried at 80 ℃ for 12 hrs to remove ethanol. The mixture was calcined successively at 700 ℃ for 2 hrs and 875 ℃ for 4 hrs. The calcined powder was ball milled in ethanol to reduce the size of particles as well as obtain uniform particle size distribution. The dried powder was pressed into pellets with a diameter of 15 mm and thickness of 1.5 mm. The pellets were sintered at 1000 ℃ for 4 hrs.

X-ray powder diffraction data were collected on a PANalytical X'Pert Pro diffractometer by using the Cu-Kα radiation (λ= 1.5418 Å) over the 2θ range 5 - 120º with a step length of 0.03342º and an effective scan time of 200 s per step. Rietveld refinements were carried out by using the GSAS software[50]. In refinements, the background was fitted by using the intercalated Chebyschev polynomial function. The scale factor, zero shift, lattice parameters and profile shapes were refined, followed by refinement of isotropic displacement parameters. The atomic occupancies were initially determined according to the chemical stoichiometry with assumption of random distributions over the doping sites. Free refinement of atomic occupancy shows close numbers to the initial values. Therefore, occupancies were then fixed in the analysis.

A scanning electron microscope (SEM, FEI, Inspect F, Hillsboro) equipped with an Energy Dispersive X-ray detector was used to observe microstructure and analyse elemental distribution within the ceramics. An X-ray photoelectron spectrometer (Nexsa, XPS system) was used to determine the chemical state of elements. To minimize signal interference from multiple absorbed species, the samples were mechanically polished and subjected to ultrasonic

cleaning in ethanol to eliminate surface contaminants. Following this, the samples were transferred into the XPS chamber, where in situ Ar^+ ion sputtering was performed under high vacuum conditions ($<3 \times 10^{-8}$ mbar) to further cleanse the surface. XPS measurement was carried out immediately after sputtering, maintaining vacuum throughout to prevent any exposure to air or re-adsorption of impurities. All XPS spectra were calibrated using C 1*s* binding energy peak at 284.8 eV.

A Scanning Probe Microscopy (SPM) system (Asylum MFP-3D Infinity, Oxford Instruments, USA) equipped with facilities for piezoresponse force microscopy (PFM), electrostatic force microscopy (EFM) and magnetic force microscopy (MFM) under external electrical and magnetic fields was employed to investigate local piezoelectric, ferroelectric and magnetic properties, and intrinsic magnetoelectric coupling at room temperature. A variable Field Module (VFM4, Oxford Instruments, USA) was employed to generate steady external magnetic field. The PFM images were acquired after reaching the required magnetic field and holding for 3 mins.

For the dielectric, ferroelectric and piezoelectric measurements, the ceramic disks were coated on both major surfaces with silver paste (Sigma-Aldrich). The Ag electrodes were fired at 650 ℃ for 20 min. The electrical displacement (D) -electric field (E)-electric current (I) loops were measured using a ferroelectric tester (NPL, Teddington, UK). The ceramics were poled in silicone oil under an electric field of 60 kV/cm for 10 minutes at room temperature, prior to dielectric property measurements. The temperature and frequency dependencies of electrical capacitance and loss tangent of the poled and unpoled ceramics were obtained with an LCR meter (Agilent Technologies Ltd, 4284A) electrically connected to a high-temperature furnace.

The magnetic field-dependent magnetization data were collected using a magnetic property measurement system (a model MPMS-XL-5, Quantum Design, USA). The

magnetoelectric coupling effect was investigated by measuring the frequency dependence of the complex dielectric permittivity and complex magnetic permeability in the GHz range with a vector network analyser (VNA, Agilent E8363B).

Declaration of Competing Interest

The authors declare no conflicts of interest.

Acknowledgements

M. Z. acknowledges the financial support from the Royal Society of Chemistry R24-1199482977; V. K. acknowledges support from the Grant Agency of the Slovak Academy of Sciences (Grant No 2/0034/23); C. J. acknowledges support from the National Natural Science Foundation of China (Nos. 12174164 and 12247101), the 111 Project under Grant No. B20063, and the Key R&D Project of Gansu Province (No. 22YF7WA014); H. Y. acknowledges the financial support from the Royal Society for a Newton Advanced Fellowship award (No. NAF\R1\201126). Y. Y. acknowledges the financial support from Guangdong Basic and applied Basic Research Foundation (No.2022A1515110210).

References

1. Scott, J. F. Room-temperature multiferroic magnetoelectrics. *NPG Asia Mater* **5**, e72 (2013).
2. Dong, S., Liu, J. M., Cheong, S. W. & Ren, Z. Multiferroic materials and magnetoelectric physics: Symmetry, entanglement, excitation, and topology. *Adv Phys* **64**, 519–626 (2015).
3. Ponet, L. *et al.* Topologically protected magnetoelectric switching in a multiferroic. *Nature* **607**, 81–85 (2022).
4. Spaldin, N. A. & Ramesh, R. Advances in magnetoelectric multiferroics. *Nat Mater* **18**, 203–212 (2019).
5. Giraldo, M. *et al.* Magnetoelectric coupling of domains, domain walls and vortices in a multiferroic with independent magnetic and electric order. *Nat Commun* **12**, 1–7 (2021).
6. Zhu, T. *et al.* Directed synthesis of a hybrid improper magnetoelectric multiferroic material. *Nat Commun* **12**, 1–8 (2021).

7. Heron, J. T. *et al.* Deterministic switching of ferromagnetism at room temperature using an electric field. *Nature* **516**, 370–373 (2014).

8. Sosnowska, I., Neumaier, T. P. & Steichele, E. Spiral magnetic ordering in bismuth ferrite. *Journal of Physics C: Solid State Physics* **15**, 4835–4846 (1982).

9. Hill, N. A. Why are there so few magnetic ferroelectrics? *Journal of Physical Chemistry B* **104**, 6694–6709 (2000).

10. Ishizaka, K. *et al.* Giant Rashba-type spin splitting in bulk BiTeI. *Nat Mater* **10**, 521–526 (2011).

11. Santander-Syro, A. F. *et al.* Giant spin splitting of the two-dimensional electron gas at the surface of $SrTiO_3$. *Nat Mater* **13**, 1085–1090 (2014).

12. Ast, C. R. *et al.* Giant spin splitting through surface alloying. *Phys Rev Lett* **98**, 1–4 (2007).

13. Pavlenko, N., Kopp, T., Tsymbal, E. Y., Mannhart, J. & Sawatzky, G. A. Oxygen vacancies at titanate interfaces: Two-dimensional magnetism and orbital reconstruction. *Phys Rev B Condens Matter Mater Phys* **86**, 1–13 (2012).

14. Pavlenko, N., Kopp, T., Tsymbal, E. Y., Sawatzky, G. A. & Mannhart, J. Magnetic and superconducting phases at the $LaAlO_3/SrTiO_3$ interface: The role of interfacial Ti 3d electrons. *Phys Rev B Condens Matter Mater Phys* **85**, 020407 (2012).

15. Krempaský, J. *et al.* Entanglement and manipulation of the magnetic and spin-orbit order in multiferroic Rashba semiconductors. *Nat Commun* **7**, 13071 (2016).

16. Anh, L. D., Hai, P. N. & Tanaka, M. Observation of spontaneous spin-splitting in the band structure of an n-type zinc-blende ferromagnetic semiconductor. *Nat Commun* **7**, 1–8 (2016).

17. Ramesh, R. & et al., et al. Epitaxial $BiFeO_3$ Multiferroic Thin Film Heterostructures. *ChemInform* **34**, 1719–1722 (2003).

18. Ederer, C. & Spaldin, N. A. Weak ferromagnetism and magnetoelectric coupling in bismuth ferrite. *Phys Rev B Condens Matter Mater Phys* **71**, 1–4 (2005).

19. He, C., Ma, Z. J., Sun, B. Z., Sa, R. J. & Wu, K. The electronic, optical and ferroelectric properties of $BiFeO_3$ during polarization reversal: A first principle study. *J Alloys Compd* **623**, 393–400 (2015).

20. See Supplemental Material at http:xxxx for the EDX, XRD data and frequency dependent dielectric properties of all the materials. The Supplemental Material also contains Ref [21] for XPS data fitting.

21. Wang, J., Mueller, D. N. & Crumlin, E. J. Recommended strategies for quantifying oxygen vacancies with X-ray photoelectron spectroscopy. *J Eur Ceram* **44**, 116709 (2024).

22. Hang, Q. *et al.* Structural, spectroscopic, and dielectric characterizations of Mn-doped $0.67BiFeO_3$-$0.33BaTiO_3$ multiferroic ceramics. *J Adv Ceram* **2**, 252–259 (2013).

23. Wang, T. H. *et al.* Structure, magnetic, and dielectric properties of (1-x)$BiFeO_3$-x$BaTiO_3$ ceramics. *J Appl Phys* **109** D907 (2011).

24. Leontsev, S. O. & Eitel, R. E. Dielectric and piezoelectric properties in Mn-modified (1-x)$BiFeO_3$-x$BaTiO_3$ ceramics. *J Am Ceram Soc* **92**, 2957–2961 (2009).

25. Wang, D. *et al.* $BiFeO_3$-$BaTiO_3$: A new generation of lead-free electroceramics. *J Adv Dielectr* **8**, 1–35 (2018).

26. Kiyanagi, R. *et al.* Structural and magnetic phase determination of (1 - x)$BiFeO_3$-x$BaTiO_3$ solid solution. *J Physical Soc Japan* **81**, (2012).

27. Buttner, R. H. & Maslen, E. N. Structural parameters and electron difference density in $BaTiO_3$. *Acta Crystallogr Sect B* **48**, 764–769 (1992).

28. Cross, L. E. & Cross, L. E. Relaxor ferroelectrics. *Ferroelectrics* **0193**, 241–267 (2011).

29. Zhang, M. *et al.* Phase transformations in an Aurivillius layer structured ferroelectric designed using the high entropy concept. *Acta Mater* **229**, 117815 (2022).

30. Viola, G. *et al.* Reversibility in electric field-induced transitions and energy storage properties of bismuth-based perovskite ceramics. *J Phys D Appl Phys* **45**, 355302 (2012).

31. Zhang, M. *et al.* Phase transformations in an Aurivillius layer structured ferroelectric designed using the high entropy concept. *Acta Mater* **229**, 117815 (2022).

32. Uchino, K. & Nomura, S. Critical exponents of the dielectric constants in diffused- phase-transition crystals. *Ferroelectrics* **44**, 55–61 (1982).

33. Jin, L., Li, F. & Zhang, S. Decoding the fingerprint of ferroelectric loops: Comprehension of the material properties and structures. *J Am Ceram Soc,* **97**, 1–27 (2014).

34. Shi, P. *et al.* High strain in $Bi_{0.5}Na_{0.5}TiO_3$-based relaxors by adding two modifiers featuring with morphotropic phase boundary. *Scr Mater* **218**, 114674 (2022).

35. A. L. Kholkin, K. G. Brooks, and N. S. Electromechanical properties of $SrBi_2Ta_2O_9$ thin films. *Appl Phys Lett* **71**, 2044 (1997).

36. Li, F. *et al.* Giant piezoelectricity ofSm-doped $Pb(Mg_{1/3}Nb_{2/3})O_3$-$PbTiO_3$ single crystals. *Science* ***364***, 264–268 (2019).

37. Goodenough, J. B. An interpretation of the magnetic properties of the perovskite-type mixed crystals $La_{1-x}Sr_xCoO_{3-\lambda}$. *Journal of Physics and Chemistry of Solids* **6**, 287-297 (1958).

38. Jiang, C., Jia, C., Wang, F., Zhou, C. & Xue, D. Transformable ferroelectric control of dynamic magnetic permeability. *Phys Rev B* **97**, 1–6 (2018).

39. Cazayous, M. *et al.* Possible observation of cycloidal electromagnons in $BiFeO_3$. *Phys Rev Lett* **101**, 2–5 (2008).

40. Pimenov, A. *et al.* Possible evidence for electromagnons in multiferroic manganites. *Nat Phys* **2**, 97–100 (2006).

41. Li, Y., Cao, W. Q., Yuan, J., Wang, D. W. & Cao, M. S. Nd doping of bismuth ferrite to tune electromagnetic properties and increase microwave absorption by magnetic-dielectric synergy. *J Mater Chem C Mater* **3**, 9276–9282 (2015).

42. Jiang, C., Jia, C., Wang, F., Zhou, C. & Xue, D. Transformable ferroelectric control of dynamic magnetic permeability. *Phys Rev B* **97**, 1–6 (2018).

43. Mostovoy, M. Multiferroics: different routes to magnetoelectric coupling. *npj Spintronics* **2**, 4–10 (2024).

44. Tagantsev, A. K., Sherman, V. O., Astafiev, K. F., Venkatesh, J. & Setter, N. *Ferroelectric Materials for Microwave Tunable Applications*. *Journal of Electroceramics* **11**, 5-66 (2003).

45. Bencan, A. *et al.* Atomic scale symmetry and polar nanoclusters in the paraelectric phase of ferroelectric materials. *Nat Commun* **12**, 3509 (2021).

46. Zhang, H. *et al.* Polar nano-clusters in nominally paraelectric ceramics demonstrating high microwave tunability for wireless communication. *J Eur Ceram Soc* **40**, 3996–4003 (2020).

47. Berlincourt, D. & Krueger, H. H. A. Domain processes in lead titanate zirconate and barium titanate ceramics. *J Appl Phys* **30**, 1804–1810 (1959).

48. Shen, Z. *et al.* Ferroelectric ceramics with enhanced remnant polarization by ordered coalescence of nano-crystals. *J Mater Chem* **22**, 23547–23552 (2012).

49. Hassanpour, E. *et al.* Magnetoelectric transfer of a domain pattern. *Science (1979)* **377**, 1109–1112 (2022).

50. Toby, B. H. EXPGUI, a graphical user interface for GSAS. *J Appl Crystallogr* **34**, 210–213 (2001).